ARTICLE

Ross Gyre variability modulates oceanic heat supply toward the West Antarctic continental shelf

Channing J. Prend [1,2✉], Graeme A. MacGilchrist[3,4], Georgy E. Manucharyan [1], Rachel Q. Pang[3], Ruth Moorman[2], Andrew F. Thompson [2], Stephen M. Griffies[3,5], Matthew R. Mazloff[6], Lynne D. Talley [6] & Sarah T. Gille [6]

West Antarctic Ice Sheet mass loss is a major source of uncertainty in sea level projections. The primary driver of this melting is oceanic heat from Circumpolar Deep Water originating offshore in the Antarctic Circumpolar Current. Yet, in assessing melt variability, open ocean processes have received considerably less attention than those governing cross-shelf exchange. Here, we use Lagrangian particle release experiments in an ocean model to investigate the pathways by which Circumpolar Deep Water moves toward the continental shelf across the Pacific sector of the Southern Ocean. We show that Ross Gyre expansion, linked to wind and sea ice variability, increases poleward heat transport along the gyre's eastern limb and the relative fraction of transport toward the Amundsen Sea. Ross Gyre variability, therefore, influences oceanic heat supply toward the West Antarctic continental slope. Understanding remote controls on basal melt is necessary to predict the ice sheet response to anthropogenic forcing.

[1] School of Oceanography, University of Washington, Seattle, WA, USA. [2] Environmental Science and Engineering, California Institute of Technology, Pasadena, CA, USA. [3] Atmospheric and Oceanic Sciences Program, Princeton University, Princeton, NJ, USA. [4] School of Earth and Environmental Sciences, University of St Andrews, St Andrews, UK. [5] NOAA Geophysical Fluid Dynamics Laboratory, Princeton, NJ, USA. [6] Scripps Institution of Oceanography, University of California San Diego, La Jolla, CA, USA. ✉email: cprend@uw.edu

Accelerated mass loss from the Antarctic Ice Sheet (AIS) has been observed in recent years[1,2], and could contribute up to one meter of global sea-level rise by the end of the century[3]. Determining its drivers is crucial to improve future sea-level and climate projections; however, ice shelf melt exhibits notable spatiotemporal variability[4]. AIS melt has long been linked to oceanic heat from intrusions of warm Circumpolar Deep Water (CDW) onto the continental shelf[5–8]. Consequently, numerous studies have investigated on-shelf CDW transport variability, which is typically attributed to climate-driven wind anomalies[9–13]. However, cross-shelf exchange is only one factor controlling the total heat supply to the ice shelf cavities. CDW delivery to the AIS also depends on the offshore heat reservoir adjacent to the shelf break, as well as the circulation and water-mass transformations on the shelf[14–16]. The remote pathways that transfer CDW from the core of the Antarctic Circumpolar Current (ACC) to the continental slope, and their potential impact on melt rate variability, remain relatively unexplored[17].

Observational studies of CDW transport toward the AIS have typically focused on specific regions, dictated by data availability[18–20], while circumpolar investigations have relied on models and often quantify the heat flux across a specific isobath[21–23]. These studies have emphasized the spatial variability in continental shelf hydrography and its relationship to basal melting. For example, in the Pacific sector, the Ross and Amundsen/Bellingshausen Seas are often categorized as cold and warm continental shelves, respectively[24–26]. This is reflected in the minimal mass loss of the Ross Ice Shelf compared to the West Antarctic Ice Sheet (WAIS)[14,27,28]. Therefore, determining the processes that control changes in continental shelf heat content is necessary to predict future AIS mass loss. For instance, melt rates at Pine Island and Thwaites glaciers, as well as Dotson Ice Shelf, have been shown to respond to wind-driven fluctuations in CDW supply to the Amundsen Sea Embayment at seasonal, inter-annual, and decadal timescales[29–33]. More recently, it was suggested that the Amundsen and Bellingshausen continental shelves are sensitive to offshore CDW properties, which are influenced by the large-scale atmospheric and oceanic circulations[17]. However, the mechanisms that connect open ocean variability with changes in continental shelf properties and ice shelf mass loss are not well constrained.

Here, we investigate remote controls on oceanic heat delivery to the AIS by characterizing CDW pathways from the ACC to the continental slope, which precede on-shelf heat transport[15,22,23]. Using Lagrangian particle release experiments in a state estimate with active mesoscale eddies[34], we show that changes in the extent and strength of the Ross Gyre mediate the magnitude and distribution of CDW transport toward the continental shelf throughout the Pacific sector of the Southern Ocean. Gyre expansion is associated with an increased southward flux of CDW via the gyre's eastern limb and a greater fraction of the heat associated with this layer moving toward the Amundsen and Bellingshausen Seas. The off-shelf heat availability to the WAIS is, therefore, regulated by interannual variations in the gyre circulation, which are caused by large-scale changes in the winds and sea ice state. Ultimately, heat delivery to the ice shelf cavities will also depend on the cross-shelf exchange and shelf circulation[15,16,35]. Still, the Ross Gyre, despite its distance from the WAIS, may be important to understanding the ice sheet's response to changes in forcing[36].

Results

Ross Gyre variability. The cyclonic Ross Gyre is forced by a clockwise (negative) wind stress curl and dominates the circulation south of the ACC in the western Pacific sector of the Southern Ocean[37,38]. The gyre acts as a conduit between the open ocean and the Antarctic margins, carrying CDW poleward to the continental slope on its eastern edge and exporting shelf waters equatorward along its western flank[39]. Given the difficulty of collecting in situ observations in this vast, seasonally ice-covered region, our understanding of the gyre dynamics stems primarily from satellite altimetry and numerical models[40–42]. In this work, we combine available observations with a dynamically consistent model by analyzing the Biogeochemical Southern Ocean State Estimate (B-SOSE)[34], a data-assimilating simulation that constrains a general circulation model with satellite and hydrographic measurements. The configuration used here has 1/6° nominal resolution (~ 8 km) and covers the period from 2013 to 2018 (Methods). Earlier iterations of this model have been used to investigate Ross Gyre transport and its relationship to the thermohaline structure of the region[38,43]. As such, we have confidence in the model's representation of the gyre circulation. For example, the expression of the gyre is visible from its relatively cold temperature on CDW isopycnal surfaces[44] (Fig. 1a).

Defining a precise gyre boundary is nontrivial. From altimetry, the boundary is typically derived from dynamic ocean topography[37,40], or implicitly the surface geostrophic flow. Here, we leverage the model's additional subsurface information by determining the gyre extent from a specific contour (− 8 Sverdrup) of the barotropic streamfunction[38], which represents the depth-integrated volume transport and is calculated from the model velocity field (Methods). The position of the gyre is bounded to the south by the continental slope and to the north and west by the Pacific-Antarctic Ridge (Fig. 1b). In fact, the interaction of the ACC with bathymetry both enables the formation of a gyre and influences its circulation and transport properties[41,42]. Bottom pressure torques associated with bathymetric features, for example, are thought to be necessary to close the barotropic vorticity budget in the region[45]. While the gyre is topographically constrained for much of its course, the separation of the flow from the Pacific-Antarctic Ridge permits much greater variability in the gyre's eastern limb until the flow meets the Marie Byrd seamounts around 68°S, 130°W. (Fig. 1b). This eastern boundary steers warm CDW southward toward the continental shelf. Therefore, fluctuations in its position could alter oceanic heat delivery to the shelf break.

The strength and structure of the Ross Gyre respond to changes in the ocean surface stress[37,40], which is the force applied to the sea surface by winds and sea ice (Methods). Satellite data suggest that changes in the ocean surface stress curl cause the gyre to fluctuate at both seasonal and interannual timescales, with the leading mode of variability being linked to atmospheric forcing by the Antarctic Oscillation (or Southern Annular Mode)[40]. B-SOSE shows similar amplitude variations in gyre transport and area, which are highly correlated to the ocean surface stress curl over the central gyre (Fig. 2a; Supplementary Figs. 1, 2). The high correlation (r=0.73) at monthly timescales indicates that the barotropic response to the ocean surface stress curl is nearly instantaneous. While the relationship between the strength of the forcing and the gyre transport is straightforward, the mechanisms that set the location of the gyre's eastern boundary, and associated variations in southward CDW transport, are less clear.

To characterize the impact of interannual variations in Ross Gyre dynamics on poleward heat flux, we select 2014 and 2018 (hereafter referred to as end-member years) as case studies of contracted and expanded gyre states, respectively. The contrast between these years is reflected in the barotropic streamfunction, which exhibits substantial differences in magnitude and extent (Fig. 2b, c). The gyre's northern and southern boundaries track f/h contours, where f is the Coriolis parameter and h is depth. Greater cyclonic vorticity input by the winds in 2018, which is
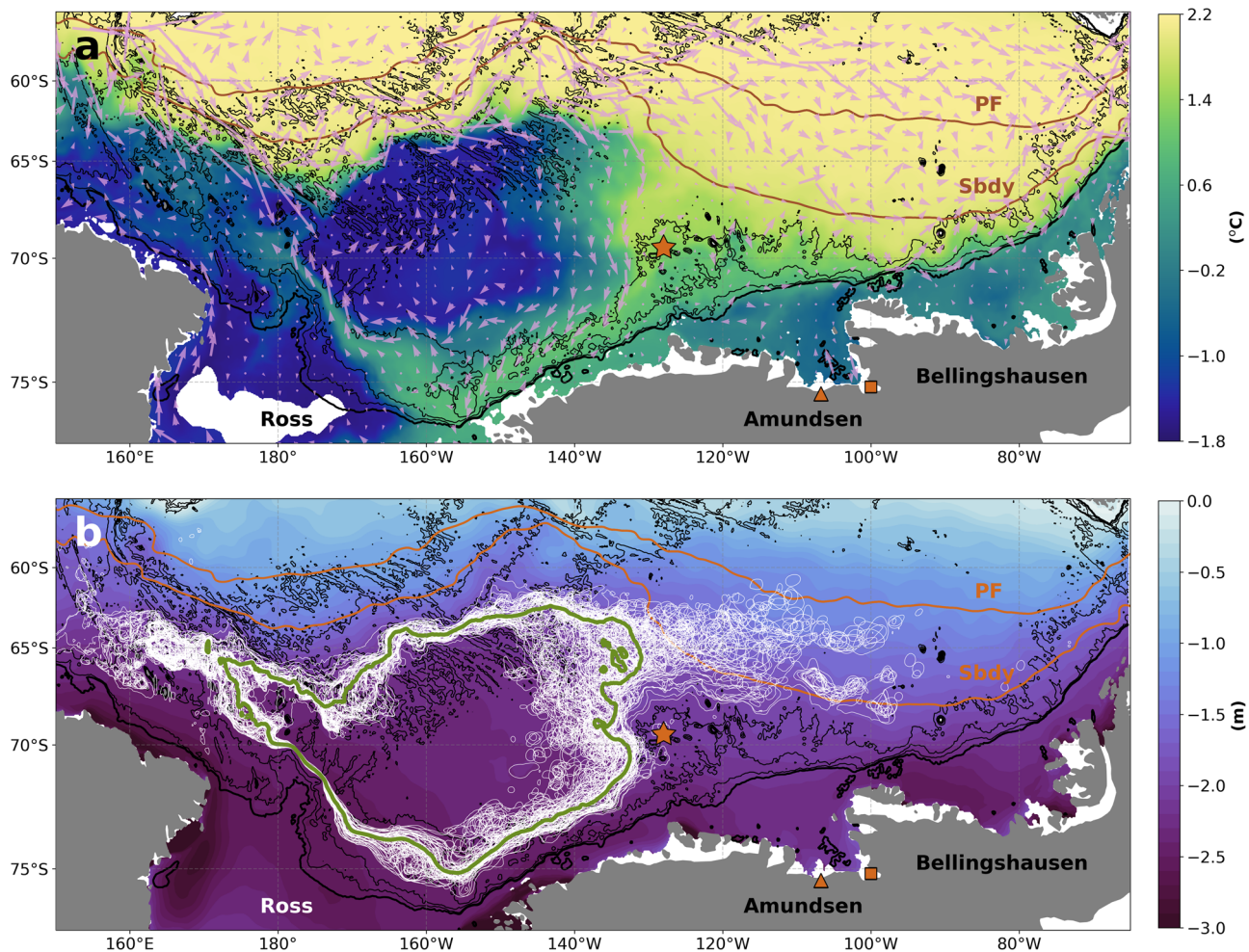
Fig. 1 Circumpolar Deep Water temperature and time-varying Ross Gyre boundary. 2013–2018 mean **a** temperature (shading) and velocity (pink arrows) on the $\gamma_n = 27.9$ kg m^{-3} neutral density surface, which corresponds to the core of the Circumpolar Deep Water layer in the model (the white region in the central Ross shelf is where the density surface outcrops), and **b** sea surface height (shading) and Ross Gyre boundary (green contour), as well as monthly realizations of the gyre boundary (white contours), which is defined by the − 8 Sverdrup contour of the barotropic streamfunction. In both panels, black contours mark bathymetry in 1000 m intervals with the 1000 m isobath plotted thicker to indicate the approximate location of the Antarctic Slope Front. Brown lines denote the Polar Front (PF) and Southern Boundary of the Antarctic Circumpolar Current (Sbdy)[60], a brown star marks the Marie Byrd seamounts, and a brown triangle and square mark the locations of Thwaites and Pine Island glaciers, respectively.

enabled by anomalously low sea ice concentrations in that year (Supplementary Fig. 3), spins up the gyre and shifts its outer bound to an f/h value that is larger in magnitude (black contours in Fig. 2b, c). This corresponds to a more northward separation of the flow from the Pacific-Antarctic Ridge and an eastward shift of the gyre's eastern boundary (blue shading in Fig. 2c). Downstream of the separation, the current crosses f/h contours, similar to standing meander regions in the ACC[46]. Just as meander curvature is related to the forcing strength[46], we suggest that the length of the gyre's barotropic streamlines should scale with the ocean surface stress curl. In other words, the eastern limb of the gyre can extend further when there is greater vorticity input by the winds. This, in turn, affects the location where heat moves toward the continental shelf.

Interannual fluctuations in gyre size co-occur with temperature and pressure anomalies on CDW isopycnal surfaces (Fig. 3). The annual mean temperature anomaly (relative to the 2013–2018 mean) on the 27.9 neutral density (γ_n) surface displays opposing patterns between the end-member years (Fig. 3a, c). The temperature properties of the CDW water mass itself do not vary on these timescales. Therefore, the isopycnic temperature anomalies indicate redistribution of heat within the system. For

example, a stronger gyre is associated with cold anomalies in the gyre interior and warm anomalies on the Amundsen continental shelf (Fig. 3a, c). This warming of the Amundsen Sea Embayment connects smoothly to offshore anomalies (Fig. 3b, d). Indeed, the offshore heat reservoir adjacent to the Amundsen undergoes a multi-year warming that is driven by a zonal heat transport convergence consistent with enhanced supply of gyre-sourced waters (Supplementary Fig. 4). We note that gyre anomalies cannot be instantaneously communicated to the shelf, and the temperature changes on the shelf will necessarily also reflect variations in onshore CDW transport. Still, fluctuations in the offshore temperature could influence the continental shelf heat content, but have received little attention previously[17]. To probe the gyre-shelf connection further, we conducted a series of Lagrangian particle release experiments to test how changes in gyre state modify the pathways of CDW transport from the ACC to the continental slope.

Particle pathways. The first set of experiments involves releasing particles on CDW density surfaces at different locations along the continental slope and running them backward in time over the full 6-year model run to diagnose where the waters originated
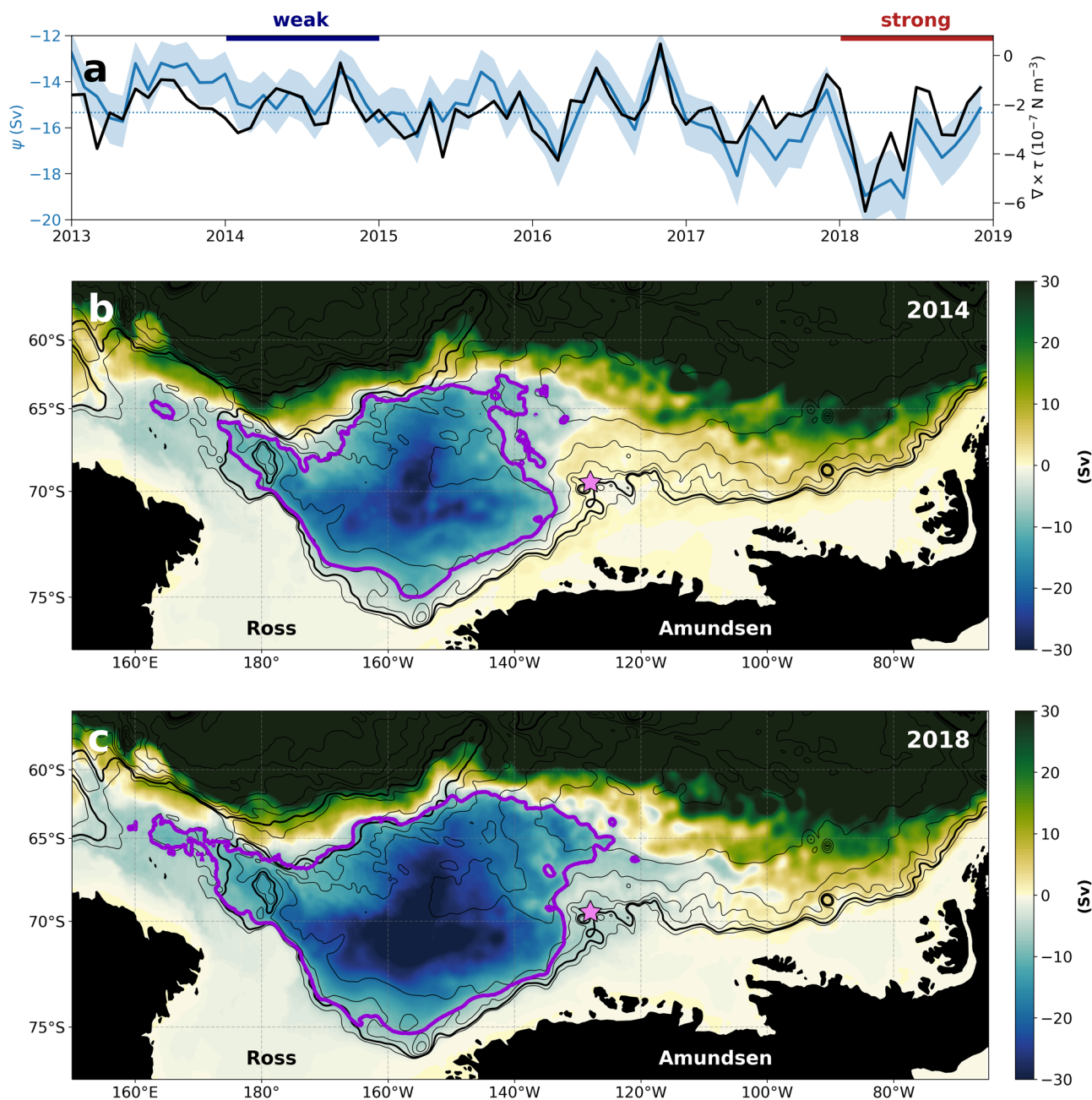
Fig. 2 Ross Gyre structure, variability, and forcing. a Monthly time series of gyre strength (blue), defined as the mean value of the barotropic streamfunction within the − 8 Sverdrup contour (which is outlined in purple in **b**, **c**), and ocean surface stress curl (black) averaged over the central gyre (140 to 152°W, 70 to 73°S, see Supplementary Fig. 1). A dashed horizontal line marks the mean gyre strength over the full record and error bars denote the standard error. **b** 2014 (weak gyre) and **c** 2018 (strong gyre) mean barotropic streamfunction (shading), with f/h contours overlaid (black). A pink star shows the location of the Marie Byrd seamounts.

(Methods). This is intended to contextualize past studies on cross-shelf exchange, which have focused on transport across the 1000 m isobath[15,22]. Comparing release locations in the Ross and Amundsen Seas (Supplementary Fig. 5) illustrates the gyre's role in poleward heat transfer. CDW moves south along the eastern flank of the gyre and separates into two distinct streams where the flow bifurcates around the Marie Byrd seamounts. One of these streams follows the gyre's westward near-slope flow, while the other proceeds to the southeast toward the Amundsen continental shelf. These two routes are associated with different timescales and degrees of watermass transformation. Particles that end up in the Ross Sea have cooled substantially after the flow bifurcates, while particles that enter the Amundsen Sea

contain relatively unmodified CDW (Fig. 4d). These results support the role of far-field processes in setting the distinct hydrographic characteristics of the Ross and Amundsen continental shelves[24].

To assess how particle pathways are affected by gyre variability, we conducted two additional experiments based around the strong and weak end-member years. Namely, we used the same release locations and 6-year backward integration, but looped the model velocity output from 2014 and 2018 to represent cases where the gyre is fixed in a contracted and expanded state. It should be noted that particles take several years to move from the ACC to the continental slope, so these looped scenarios do not reflect realistic trajectories. Nevertheless, they provide
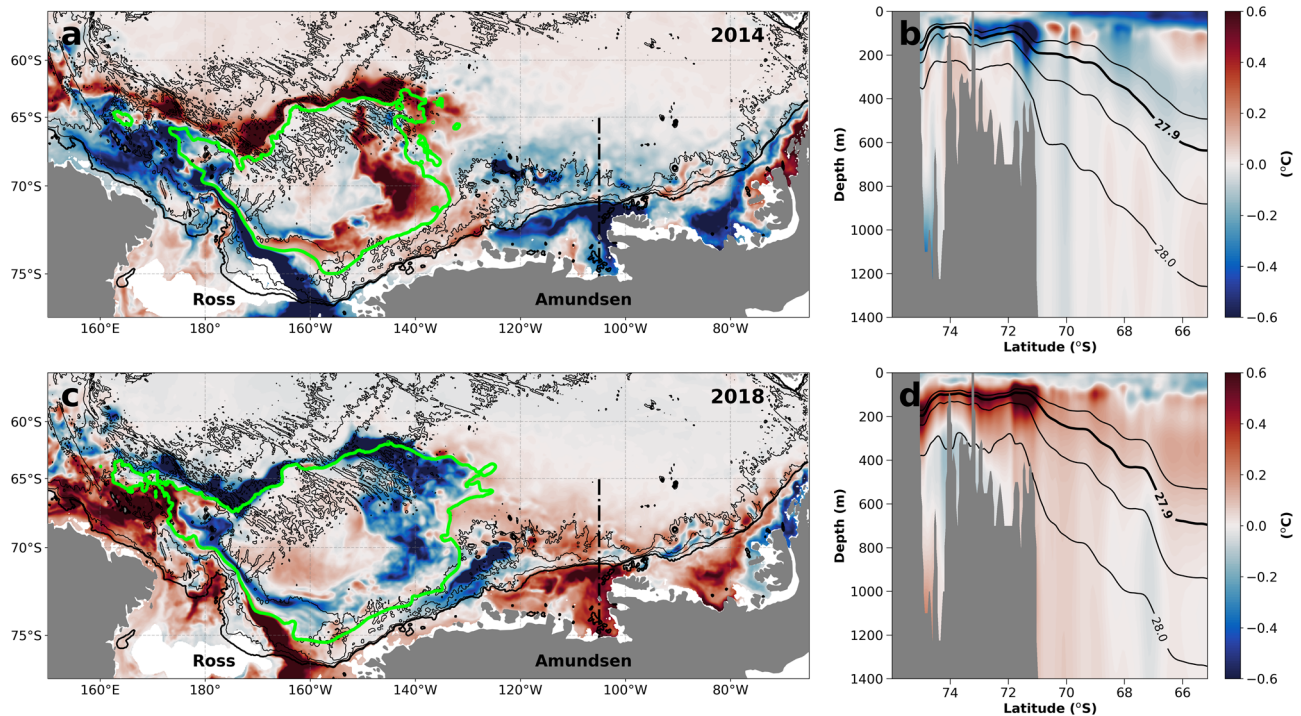
Fig. 3 Ocean temperature anomalies associated with contracted and expanded gyre states. Map of the annual mean temperature anomaly (relative to the 2013-2018 mean) on the $\gamma_n = 27.9\,\text{kg}\,\text{m}^{-3}$ surface for **a** 2014 and **c** 2018, reflecting the contracted and expanded gyre states, respectively. In both panels, the green contour represents the mean gyre boundary for that year, while black contours mark bathymetry in 1000 m intervals with the 1000 m isobath plotted thicker to indicate the approximate location of the Antarctic Slope Front. The dashed black line indicates a meridional transect moving offshore from the Amundsen Sea continental shelf (along 105°W). The annual mean temperature anomaly in the top 1400 m on this transect is plotted for **b** 2014 and **d** 2018. Black contours denote isopycnals for each year, with the 27.9 γ_n surface highlighted in bold.

mechanistic insight into how gyre extent affects the particle pathways. An expanded and strengthened gyre (Fig. 4c) provides a closer connection between the gyre's eastern limb and the Amundsen Sea, which results in more unmodified CDW from the ACC reaching the continental slope (Fig. 4d). A stronger gyre also more directly links the open ocean and the Ross continental shelf, with less meandering and mixing of waters in the near-slope flow after the bifurcation at the Marie Byrd seamounts. This linkage is evidenced by the shift toward zero in the probability density function of cumulative temperature change along a trajectory (Fig. 4d).

In order to quantify the partitioning of particles between the two routes, we conducted a forward particle release experiment along a transect that extends from 130 to 135°W at 67°S—capturing the core of the gyre's eastern limb. The meridional heat transport through this transect exhibits interannual variability, with a greater southward flux throughout the CDW density layer in 2018, when the gyre was stronger (Fig. 5b). The increased heat transport is primarily due to the higher current speeds associated with a stronger gyre, rather than changes in the temperature profile itself (Supplementary Fig. 6). Differences in gyre state also lead to changes in the pathways of poleward flow. This can be seen by comparing trajectories from particles that were advected by the 2014 (Fig. 5a) and 2018 (Fig. 5c) velocity fields, using the same looping technique described previously. Gyre expansion favors the movement of particles toward the Amundsen Sea (Fig. 5c), as compared to the mean state (Supplementary Fig. 7).

To demonstrate the redistribution of particles between the two streams around the Marie Byrd seamounts, we can examine the fraction of particles that travel eastward from their initial release location along the transect, which varies greatly in depth and between the end-member years (Fig. 5d). For particles seeded

between 400 and 800 m, corresponding to Upper CDW, an expanded gyre roughly doubles the percentage of trajectories that move toward the Amundsen and Bellingshausen continental shelves. This reorganization is linked to changes in the position of the gyre's eastern limb, especially the location where it meets the Marie Byrd seamounts, which controls the bifurcation of the flow. Furthermore, the substantial depth dependence of the partitioning implies that the flow is not barotropic. In particular, the relatively abrupt change within the thermocline (~ 700 m in Fig. 5d) suggests that this is a first baroclinic mode response. The gyre's baroclinic structure is largely unknown since our understanding of the gyre dynamics stems primarily from satellite altimetry[37,40]. While the variability in gyre strength is well-explained by the rapid barotropic response to changes in ocean surface stress curl (Fig. 2a), the Lagrangian trajectories suggest that baroclinic adjustments can be important at longer (multi-year) timescales.

Conclusions
Predicting future WAIS melt is crucial to constrain sea-level rise projections[3], which, in turn, inform policy to address climate impacts. Improved prediction requires better knowledge of the processes that transfer heat from the open ocean to the ice shelf cavities[14]. While many studies have examined cross-shelf heat fluxes[15,22,23,47], comparatively few have considered the pathways that bring CDW from the ACC to the continental slope[17]. Here, we have shown, using a data-assimilating state estimate, that Ross Gyre variability impacts the magnitude and distribution of oceanic heat supply toward the continental shelf. This connection arises from variations in the position of the gyre's eastern limb, which is responsible for transporting CDW to the shelf break. An expanded gyre preferentially steers heat toward the Amundsen
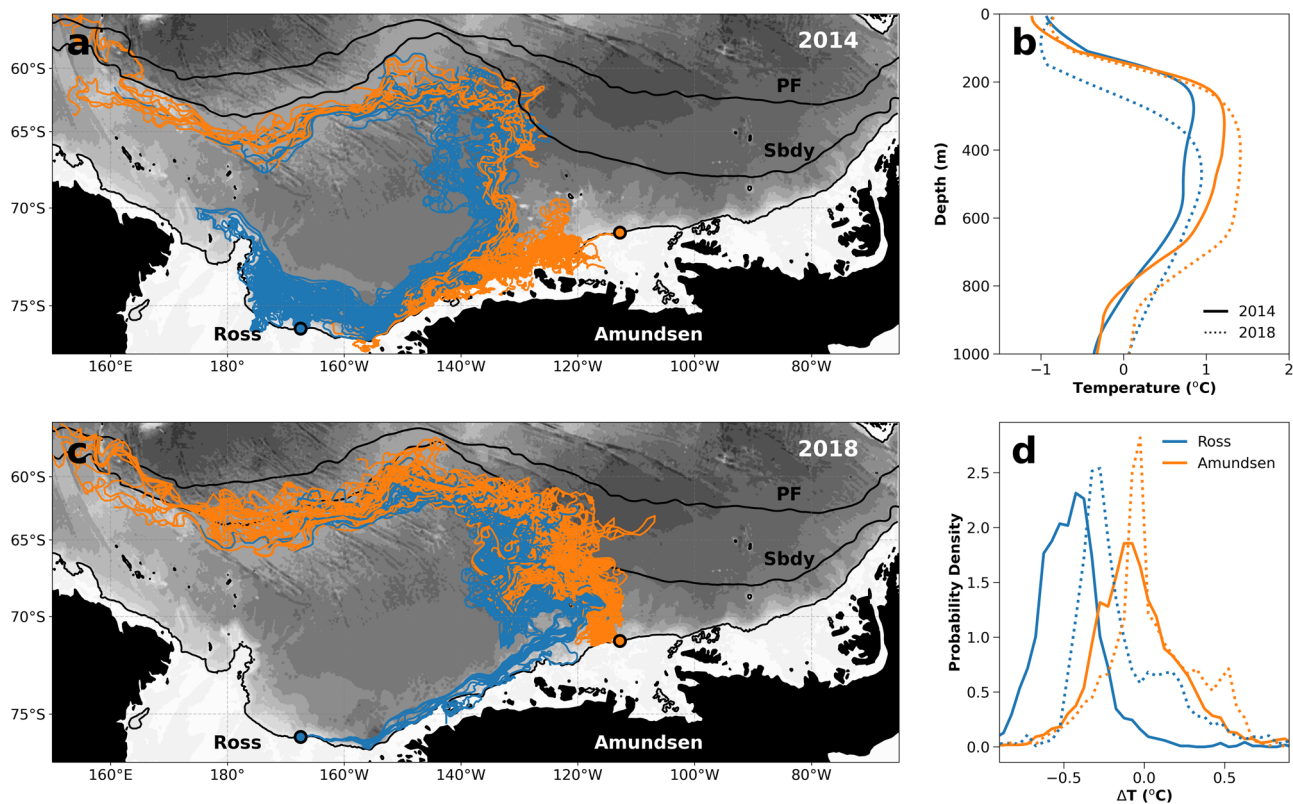
Fig. 4 Reverse particle trajectories showing differences in the origin of continental slope waters during contracted and expanded gyre states. 100 randomly selected trajectories for particles released at the contentinal slope in the Ross (blue) and Amundsen (orange) and run backwards with the **a** 2014 (weak gyre) and **c** 2018 (strong gyre) velocity fields, looped to achieve a 6-year integration time. Underlying shading denotes bathymetry and black lines mark the 1000 m isobath, Polar Front (PF) and Southern Boundary of the Antarctic Circumpolar Current (SBdy)[60]. **b** Vertical temperature profiles at the release locations (circles in **a** and **c**) in the Ross (blue) and Amundsen (orange) sectors for 2014 (solid) and 2018 (dotted). **d** Probability density functions of the cumulative temperature change along a trajectory for the Ross (blue) and Amundsen (orange) particles for 2014 (solid) and 2018 (dotted) looped velocities.

and Bellingshausen Seas, leading to a zonal heat transport convergence that warms the subsurface waters offshore of the Amundsen continental shelf (Fig. 6c). These results suggest a possible link between Ross Gyre size and melt rates for West Antarctic ice shelves.

It is important to recognize, however, that other processes affect the eventual heat delivery to the ice shelf cavities. These include the on-shelf CDW flux[11,12] and the shelf circulation[16,48,49], both of which exhibit variability—in some cases due to the same atmospheric forcing that drives the gyre[10,32]. Variability in the thickness of the CDW layer at the Amundsen Sea Embayment is typically attributed to the zonal winds at the shelf break (yellow box in Fig. 6a). Eastward wind anomalies in this location have been shown to enhance onshore CDW transport at interannual timescales due to barotropic acceleration of the Amundsen undercurrent[9,11,50]. However, the opposite relationship between winds and cross-shelf heat flux has been observed at decadal timescales, which was linked to baroclinic adjustment of the undercurrent[8]. The interaction of these mechanisms with Ross Gyre variability has not been explored, although large-scale sea level pressure differences between the end-member years (Fig. 6a) would presumably influence both the gyre forcing and the wind-driven onshore transport.

To begin assessing this relationship, we can examine, in concert, the ocean surface stress curl over the central gyre and the zonal wind anomalies at the Amundsen shelf break. The two are weakly correlated ($r = 0.19$) at monthly timescales (Fig. 6b), suggesting that the gyre conditions that preferentially steer CDW toward the Amundsen may also be associated with enhanced on-

shelf CDW transport. Note that this conclusion is independent of the model's explicit representation of cross-shelf exchange. Ultimately, quantifying the full pathways of CDW from its origin in the ACC to the ice shelf itself is necessary to understand the regional response of AIS mass loss to changes in forcing. However, our focus here is on the pathways from the open ocean to the continental slope given that the horizontal grid spacing of B-SOSE is too coarse to resolve some of the dynamics relevant to cross-shelf heat transport, which has been shown to be sensitive to model resolution[23,51]. Still, we have demonstrated that Ross Gyre variability can modulate the heat reservoir offshore of the Amundsen Sea at interannual timescales and thus deserves further investigation in the context of continental shelf heat content and WAIS melt. Future work should consider how changes in gyre circulation interact with the processes that enable cross-shelf exchange across a range of timescales.

Given the 6-year length of the B-SOSE simulation, it is difficult to reach conclusions about long-term changes induced by anthropogenic forcing. Recent work projected an expansion of the Ross Gyre over the 21st century due to increased vorticity input by the winds, which led to changes in continental shelf properties in West Antarctica[36]. Another recent study projects unavoidable warming of the Amundsen continental shelf by the end of the century regardless of the forcing scenario[52]. B-SOSE has an evident trend in gyre strength and associated CDW temperature anomalies, but this could be due to subsampling decadal fluctuations. In that case, the end-member years can be thought of as representing earlier and later periods within a longer-term signal. Furthermore, due to the distance between the
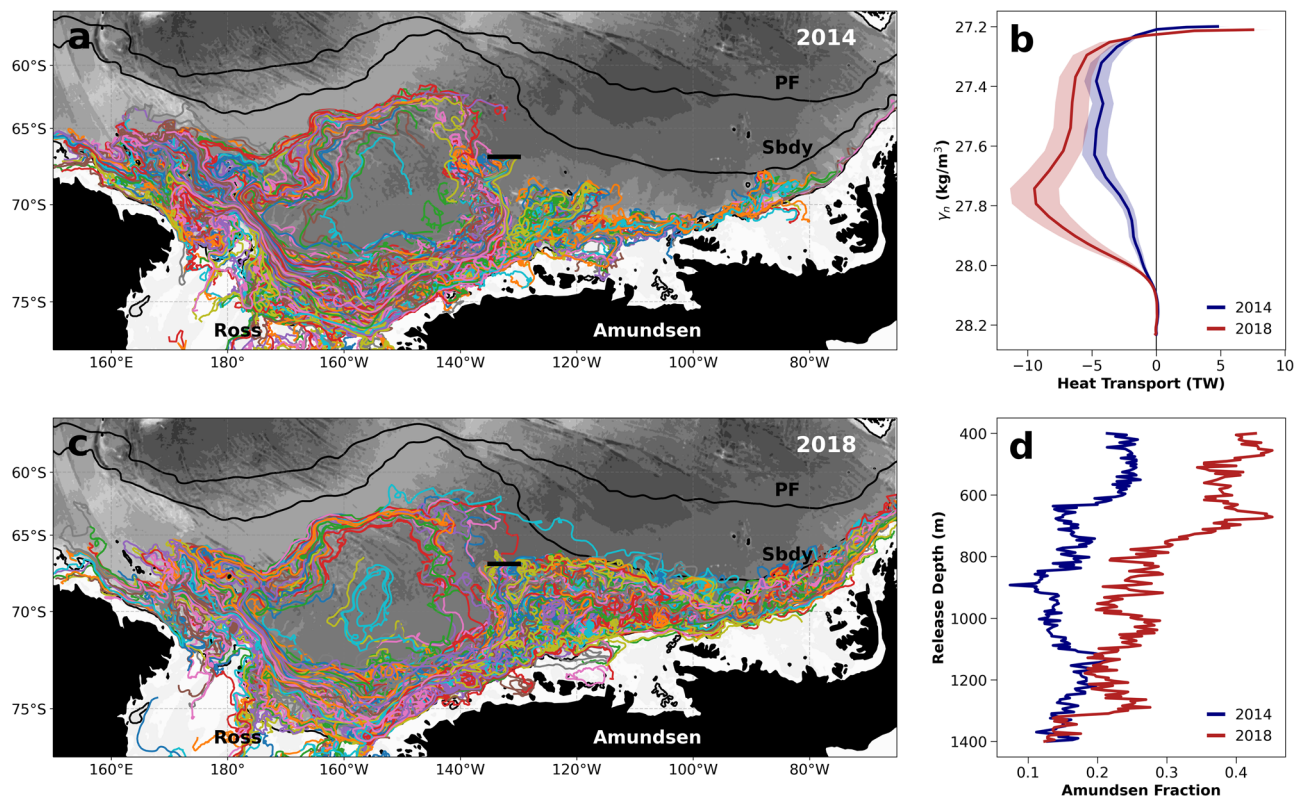
Fig. 5 Forward particle trajectories demonstrating the impact of gyre variability on poleward heat transport magnitude and spatial distribution. 500 randomly selected trajectories for particles released at 600 m along a transect that extends from 130 to 135°W at 67°S (black line) and advected by the **a** 2014 and **c** 2018 velocity fields, looped to achieve a 6-year integration time. Underlying shading denotes bathymetry and black lines mark the 1000 m isobath, Polar Front (PF) and Southern Boundary of the Antarctic Circumpolar Current (SBdy)[60]. **b** Meridional heat transport, defined relative to 0 °C, through the release transect for the two end-member years; a negative transport is southward. Error bars denote the standard error. **d** Fraction of particles that move eastward from their initial release location after 1 year (i.e. toward the Amundsen Sea), plotted as a function of release depth, for both looped velocity scenarios.

gyre and continental shelf, the anomalies on the shelf are likely related to multi-year gyre-mediated changes to the offshore heat reservoir, rather than variations in the gyre circulation in any one year specifically. Nevertheless, characterizing the expanded and contracted gyre states within the model can provide mechanistic insight that is relevant to both the natural variability and forced trend.

Record low Antarctic sea ice extent in 2023, which may indicate a shift in sea ice state[53], is expected to strengthen the gyre by permitting the winds to input greater vorticity. Additionally, future changes to Southern Ocean winds and the Amundsen Sea Low under climate forcing[54] also favor conditions for gyre expansion. These results imply enhanced warming of the offshore heat reservoir adjacent to the Amundsen in the coming decades, and potentially a greater importance of the Ross Gyre and open ocean sea ice anomalies to the temperature variability on the continental shelf. Moreover, if this offshore warming co-occurs with the same or greater magnitude of onshore volume transport, then we would expect accelerated melting of the most vulnerable ice shelves in West Antarctica, including those that buttress Pine Island and Thwaites glaciers. Further work addressing these possible feedbacks is urgently needed given the broad ramifications of constraining future WAIS melt for climate prediction.

Methods

This study investigates pathways of CDW transport using the data-assimilating Biogeochemical Southern Ocean State Estimate (B-SOSE)[34], which constrains the Massachusetts Institute of Technology general circulation model (MITgcm) solution[55] with satellite and hydrographic measurements. The configuration used in this analysis, Iteration 133, has 1/6° horizontal grid spacing (~8 km), 52 uneven vertical levels, and runs from 1 January 2013 to 31 December 2018. The model assimilates ocean observations, including satellite data, shipboard CTD measurements, and Argo float profiles; bathymetry is from the ETOPO1 Global Relief Model[56]. This iteration of B-SOSE is publicly available (http://sose.ucsd.edu).

Here, we define the Ross Gyre using the barotropic streamfunction, or the depth-integrated volume transport, which is calculated by integrating the model velocity field northward from the coast and vertically[38]. Specifically, we use the -8 Sverdrup (10^6 m^3 s^{-1}) contour of the streamfunction as the gyre boundary, following Roach & Speer (2019), which used this definition to investigate Ross Gyre dynamics using an earlier iteration of the same model. Aside from the maps illustrating the gyre boundary (Figs. 1b, 3a, c) and the calculation of gyre strength (Fig. 2a), the analysis does not rely on this -8 Sverdrup value. Furthermore, the temporal gyre variability is strongly correlated (r > 0.98) for a range of threshold values (Supplementary Fig. 8), and the results from the Lagrangian particle release experiments are independent of any particular gyre boundary definition. The error bars for gyre strength in Fig. 2a reflect the standard error of the monthly means based on the model's 5-day velocity fields.

To investigate the drivers of gyre variability, we consider the ocean surface stress—the force applied to the ocean surface by the winds and sea ice—defined as $\tau = \alpha \tau_{\text{ice-ocean}} + (1 - \alpha)\tau_{\text{air-water}}$, where α is the sea ice concentration, $\tau_{\text{ice-ocean}}$ is the ice-ocean
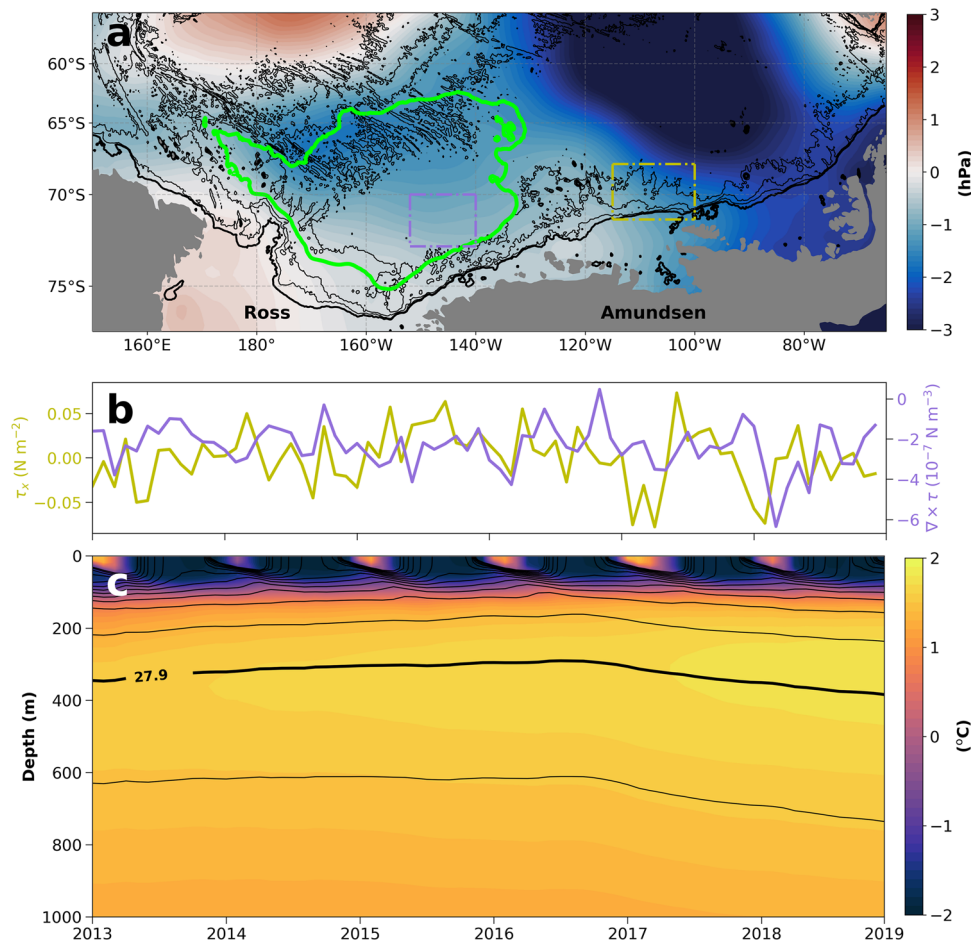
Fig. 6 Comparison of Ross Gyre forcing and Amundsen continental shelf break winds that drive onshore transport variability. a 2018 minus 2014 sea level pressure, with a green contour denoting the mean gyre boundary and black lines marking bathymetry in 1000 m intervals with the 1000 m isobath plotted thicker to indicate the approximate location of the Antarctic Slope Front. A purple box denotes the region of maximum negative wind stress curl that forces the gyre and a yellow box marks the offshore heat reservoir adjacent to the Amundsen. **b** Monthly time series of zonal wind stress anomaly (yellow) near the Amundsen continental slope (yellow box in **a**) and ocean surface stress curl (purple) averaged over the gyre forcing region (purple box in **a**). **c** Time series of upper ocean temperature in the offshore reservoir (yellow box in **a**) with isopycnals overlaid in black and the 27.9 γ_n surface highlighted in bold.

stress, and $\tau_{\text{air}-\text{water}}$ is the wind stress. The ocean surface stress is diagnosed directly in the model, and thus does not require additional calculation. However, we write out the expression here to highlight the fact that the ocean surface stress is not equivalent to the wind stress in the presence of sea ice. In fact, the increase in ocean surface stress curl over the central gyre that drives the gyre expansion is due largely to negative sea ice concentration anomalies in the region (Supplementary Fig. 3) rather than variability in the wind stress.

To illustrate the isopycnic temperature variability associated with the contracted and expanded gyre states, we plot the 2014 and 2018 annual mean temperature anomaly on the $\gamma_n = 27.9$ kg m^{-3} surface (Fig. 3a,c). This isopycnal was selected since it corresponds to the subsurface temperature maximum at the shelf break in the Amundsen (marked by an orange circle in Fig. 4a, c), and is thus taken to be the core of the CDW layer in the model. However, the subsurface layer of warmer temperatures at this location is broad and spans a range of densities and depths (Fig. 4b). Indeed, CDW is known to be comprised of several density classes. While we assume throughout that CDW is isolated from surface forcing, we note that the 27.9 γ_n surface outcrops in winter in a small region within the central gyre (Supplementary Fig. 9). Although, this does not correspond to the locations with the largest isopycnic temperature anomalies,

which occur due to shifting of the strong isopycnal temperature gradient near the gyre edge (visible in Fig. 1a). This gradient is present on denser surfaces as well, so the isopycnic temperature anomaly patterns look qualitatively similar for $\gamma_n = 28.0$ kg m^{-3} (Supplementary Fig. 10). We present the 27.9 γ_n surface in the main text since it corresponds to the subsurface temperature maximum at the shelf break, which suggests its relevance to the onshore heat transport. However, the conclusions of the paper do not depend on the selection of this particular density surface.

B-SOSE 5-day mean velocity fields were used to calculate offline Lagrangian particle trajectories using the particle-tracking model Parcels, which is available online (http://oceanparcels.org/). Details of the interpolation scheme have been described previously[57,58]. For the purposes of this study, we conducted 3 reverse and 3 forward release experiments. Here, we are interested in subsurface pathways, so we only consider particles that do not outcrop into the mixed layer. The reverse releases were done by seeding 2,500,000 particles at different locations along the 1000 m isobath (Supplementary Fig. 5) and at all depths in the water column. Particles were first released at the end of the simulation (i.e. December 31, 2018) and integrated backwards in time for 6 years to the beginning of the model run. Two other experiments were done with the same initial locations and 6-year integration time. However, instead of using the full model

velocity field, we loop 2014 and 2018 velocities to represent contracted and expanded gyre states, respectively.

The forward particle releases were done along a transect that extends from 130 to 135°W at 67°S. The meridional heat transport across this transect was calculated as $\iint \rho c_p T v \, dA \, dz$ using constants for ρ (1027 kg m^{-3}) and c_p (3990 J kg^{-1}°C^{-1}), along with the model temperature (T) and meridional velocity (v) fields. The transport is defined relative to 0°C[59], therefore, when the temperature is negative, a southward heat transport corresponds to a northward mass transport of water less than 0°C. However, we note that temperatures are always positive within the relevant CDW density range, so the heat transport is in the same direction as the mass transport. Error bars in Fig. 5b and Supplementary Fig. 4 reflect the standard error of the annual means based on the monthly transports.

The magnitude of the heat transport across this transect does depend on the precise segment location and width, however the poleward heat transport is enhanced in 2018 (expanded gyre) relative to 2014 (contracted gyre) regardless of position, although the longitude of the maximum heat transport does shift (Supplementary Fig. 11). As such, we release particles along a transect, rather than from a point location, in order to capture the core of the gyre's eastern limb, even as it changes position in time. For the release experiment, we seeded 100,000 particles evenly spaced along the transect at all depths between 400 and 1400 m, which includes both the Upper and Lower Circumpolar Deep Water layers at this location. Particles were first released at the beginning of the simulation (i.e. January 1, 2013) and integrated forward in time for 6 years to the end of the model run (Supplementary Fig. 7). Similar to above, we also computed trajectories for the same release locations, but looping the 2014 and 2018 velocities (Fig. 5a, c).

Data availability

References

1. Paolo, F. S., Fricker, H. A. & Padman, L. Volume loss from Antarctic ice shelves is accelerating. *Science* **348**, 327–331 (2015).
2. Konrad, H. et al. Net retreat of Antarctic glacier grounding lines. *Nat. Geosci.* **11**, 258–262 (2018).
3. Edwards, T. L. et al. Projected land ice contributions to twenty-first-century sea level rise. *Nature* **593**, 74–82 (2021).
4. Adusumilli, S., Fricker, H. A., Medley, B., Padman, L. & Siegfried, M. R. Interannual variations in meltwater input to the Southern Ocean from Antarctic ice shelves. *Nat. Geosci.* **13**, 616–620 (2020).
5. Rignot, E. & Jacobs, S. S. Rapid bottom melting widespread near Antarctica Ice Sheet grounding lines. *Science* **296**, 2020–2023 (2002).
6. Payne, A. J., Vieli, A., Shepherd, A., Wingham, D. J. & Rignot, E. Recent dramatic thinning of largest west Antarctic ice stream triggered by oceans. *Geophys. Res. Lett.* **31**, L23401 (2004).
7. Rintoul, S. R. et al. Ocean heat drives rapid basal melt of the Totten Ice Shelf. *Sci. Adv.* **2**, e1601610 (2016).
8. Silvano, A. et al. Baroclinic ocean response to climate forcing regulates decadal variability of ice-shelf melting in the Amundsen Sea. *Geophys. Res. Lett.* **49**, e2022GL100646 (2022).
9. Dutrieux, P. et al. Strong sensitivity of Pine Island ice-shelf melting to climatic variability. *Science* **343**, 174–178 (2014).
10. Jenkins, A. et al. West Antarctic Ice Sheet retreat in the Amundsen Sea driven by decadal oceanic variability. *Nat. Geosci.* **11**, 733–738 (2018).
11. Dotto, T. S. et al. Wind-driven processes controlling oceanic heat delivery to the Amundsen Sea, Antarctica. *J. Phys. Oceanogr.* **49**, 2829–2849 (2019).
12. Christie, F. D. W., Steig, E. J., Gourmelen, N., Tett, S. F. B. & Bingham, R. G. Inter-decadal climate variability induces differential ice response along Pacific-facing West Antarctica. *Nat. Commun.* **14**, 93 (2023).
13. Morrison, A. K. et al. Sensitivity of Antarctic shelf waters and abyssal overturning to local winds. *J. Clim.* **36**, 1–32 (2023).
14. Nakayama, Y. et al. Pathways of ocean heat towards Pine Island and Thwaites grounding lines. *Sci. Rep.* **9**, 16649 (2019).
15. Morrison, A. K., Hogg, A. M., England, M. H. & Spence, P. Warm Circumpolar Deep Water transport toward Antarctica driven by local dense water export in canyons. *Sci. Adv.* **6**, eaav2516 (2020).
16. Tamsitt, V., England, M. H., Rintoul, S. R. & Morrison, A. K. Residence time and transformation of warm Circumpolar Deep Water on the Antarctic Continental Shelf. *Geophys. Res. Lett.* **48**, e2021GL096092 (2021).
17. Nakayama, Y., Menemenlis, D., Zhang, H., Schodlok, M. & Rignot, E. J. Origin of Circumpolar Deep Water intruding onto the Amundsen and Bellingshausen Sea continental shelves. *Nat. Commun.* **9**, 3403 (2018).
18. Walker, D. P. et al. Oceanic heat transport onto the Amundsen Sea shelf through a submarine glacial trough. *Geophys. Res. Lett.* **34**, L02602 (2007).
19. Couto, N. C., Martinson, D. G., Kohut, J. & Schofield, O. Distribution of Upper Circumpolar Deep Water on the warming continental shelf of the West Antarctic Peninsula. *J. Geophys. Res. Oceans* **122**, 5306–5315 (2017).
20. Schulze Chretien, L. M. et al. The shelf circulation of the Bellingshausen Sea. *J. Geophys. Res. Oceans* **126**, e2020JC016871 (2021).
21. Schodlok, M. P., Menemenlis, D. & Rignot, E. J. Ice shelf basal melt rates around Antarctica from simulations and observations. *J. Geophys. Res. Oceans* **121**, 1085–1109 (2016).
22. Palóczy, A., Gille, S. T. & McClean, J. L. Oceanic heat delivery to the Antarctic Continental Shelf: large-scale, low-frequency variability. *J. Geophys. Res. Oceans* **123**, 7678–7701 (2018).
23. Stewart, A. L., Klocker, A. & Menemenlis, D. Circum-Antarctic shoreward heat transport derived from an eddy-and tide-resolving simulation. *Geophys. Res. Lett.* **45**, 834–845 (2018).
24. Thompson, A. F., Stewart, A. L., Spence, P. & Heywood, K. J. The Antarctic Slope Current in a changing climate. *Rev. Geophys.* **56**, 741–770 (2018).
25. Narayanan, A., Gille, S. T., Mazloff, M. R. & Murali, K. Water mass characteristics of the Antarctic margins and the production and seasonality of Dense Shelf Water. *J. Geophys. Res. Oceans* **124**, 9277–9294 (2019).
26. Moorman, R., Morrison, A. K. & Hogg, A. M. Thermal responses to Antarctic Ice Shelf melt in an eddy-rich global ocean-sea ice model. *J. Clim.* **33**, 6599–6620 (2020).
27. Depoorter, M. A. et al. Calving fluxes and basal melt rates of Antarctic ice shelves. *Nature* **502**, 89–92 (2013).
28. Webber, B. G. M. et al. Mechanisms driving variability in the ocean forcing of Pine Island Glacier. *Nat. Commun.* **8**, 14507 (2017).
29. Thoma, M., Jenkins, A., Holland, D. & Jacobs, S. Modelling Circumpolar Deep Water intrusions on the Amundsen Sea continental shelf, Antarctica. *Geophys. Res. Lett.* **35**, L18602 (2008).
30. Dinniman, M. S., Klinck, J. M. & Hofmann, E. E. Sensitivity of Circumpolar Deep Water transport and ice shelf basal melt along the West Antarctic Peninsula to changes in the winds. *J. Clim.* **25**, 4799–4816 (2012).
31. Spence, P. et al. Localized rapid warming of West Antarctic subsurface waters by remote winds. *Nat. Clim. Change* **7**, 595 (2017).
32. Holland, P. R., Bracegirdle, T. J., Dutrieux, P., Jenkins, A. & Steig, E. J. West Antarctic ice loss influenced by internal climate variability and anthropogenic forcing. *Nat. Geosci.* **12**, 718–724 (2019).
33. Yang, H. W. et al. Seasonal variability of ocean circulation near the Dotson Ice Shelf, Antarctica. *Nat. Commun.* **13**, 1138 (2022).
34. Verdy, A. & Mazloff, M. R. A data assimilating model for estimating Southern Ocean biogeochemistry. *J. Geophys. Res. Oceans* **122**, 6968–6988 (2017).
35. Dawson, H. R. S., Morrison, A. K., England, M. H. & Tamsitt, V. Pathways and timescales of connectivity around the Antarctic continental shelf. *J. Geophys. Res. Oceans* **128**, e2022JC018962 (2023).
36. Gómez-Valdivia, F., Holland, P. R., Siahaan, A., Dutrieux, P. & Young, E. Projected West Antarctic ocean warming caused by an expansion of the Ross Gyre. *Geophys. Res. Lett.* **50**, e2023GL102978 (2023).
37. Armitage, T. W. K., Kwok, R., Thompson, A. F. & Cunningham, G. Dynamic topography and sea level anomalies of the Southern Ocean: variability and teleconnections. *J. Geophys. Res. Oceans* **123**, 613–630 (2018).
38. Roach, C. J. & Speer, K. Exchange of water between the Ross Gyre and ACC assessed by Lagrangian particle tracking. *J. Geophys. Res. Oceans* **124**, 4631–4643 (2019).
39. Orsi, A. H. & Wiederwohl, C. L. A recount of Ross Sea waters. *Deep-Sea Res. II* **56**, 778–795 (2009).
40. Dotto, T. S. et al. Variability of the Ross Gyre, Southern Ocean: drivers and responses revealed by satellite altimetry. *Geophys. Res. Lett.* **45**, 6195–6204 (2018).

41. Patmore, R. D. et al. Topographic control of Southern Ocean gyres and the Antarctic circumpolar current: a barotropic perspective. *J. Phys. Oceanogr.* **49**, 3221–3244 (2019).

42. Wilson, E. A., Thompson, A. F., Stewart, A. L. & Sun, S. Bottom-up control of subpolar gyres and the overturning circulation in the Southern Ocean. *J. Phys. Oceanogr.* **52**, 205–223 (2022).

43. Mazloff, M. R., Heimbach, P. & Wunsch, C. An eddy-permitting Southern Ocean State Estimate. *J. Phys. Oceanogr.* **40**, 880–899 (2010).

44. Orsi, A. H., Whitworth, T. & Nowlin, W. D. On the meridional extent and fronts of the Antarctic Circumpolar Current. *Deep-Sea Res. I* **42**, 641–673 (1995).

45. Sonnewald, M., Reeve, K. A. & Lguensat, R. A Southern Ocean supergyre as a unifying dynamical framework identified by physics-informed machine learning. *Commun. Earth Environ.* **4**, 153 (2023).

46. Thompson, A. F. & Naveira Garabato, A. C. Equilibration of the Antarctic Circumpolar Current by standing meanders. *J. Phys. Oceanogr.* **44**, 1811–1828 (2014).

47. Stewart, A. L. & Thompson, A. F. Eddy-mediated transport of warm Circumpolar Deep Water across the Antarctic Shelf Break. *Geophys. Res. Lett.* **42**, 432–440 (2015).

48. Jacobs, S. S., Jenkins, A., Giulivi, C. F. & Dutrieux, P. Stronger ocean circulation and increased melting under Pine Island Glacier ice shelf. *Nat. Geosci.* **3**, 519–523 (2011).

49. Narayanan, A. et al. Zonal distribution of Circumpolar Deep Water transformation rates and its relation to heat content on Antarctic shelves. *J. Geophys. Res. Oceans* **128**, e2022JC019310 (2023).

50. Assmann, K. M. et al. Variability of Circumpolar Deep Water transport onto the Amundsen Sea continental shelf through a shelf break trough. *J. Geophys. Res. Oceans* **118**, 6603–6620 (2013).

51. St-Laurent, P., Klinck, J. M. & Dinniman, M. S. On the role of coastal troughs in the circulation of warm Circumpolar Deep Water on Antarctic Shelves. *J. Phys. Oceanogr.* **43**, 51–64 (2013).

52. Naughten, K. A., Holland, P. R. & De Rydt, J. Unavoidable future increase in West Antarctic ice-shelf melting over the twenty-first century. *Nat. Clim. Change* **13**, 1222–1228 (2023).

53. Purich, A. & Doddridge, E. W. Record low Antarctic sea ice coverage indicates a new sea ice state. *Commun. Earth Environ.* **4**, 314 (2023).

54. Hosking, J. S., Orr, A., Bracegirdle, T. J. & Turner, J. Future circulation changes off West Antarctica: Sensitivity of the Amundsen Sea Low to projected anthropogenic forcing. *Geophys. Res. Lett.* **43**, 367–376 (2016).

55. Marshall, J., Adcroft, A., Hill, C., Perelman, L. & Heisey, C. A finite-volume, incompressible Navier Stokes model for studies of the ocean on parallel computers. *J. Geophys. Res. Oceans* **102**, 5753–5766 (1997).

56. Amante, C. & Eakins, B. W.ETOPO1 1 arc-minute global relief model: procedures, data sources and analysis, NOAA Technical Memorandum NESDIS NGDC-24 (National Geophysical Data Center, NOAA, 2009).

57. Lange, M. & van Sebille, E. Parcels v0.9: prototyping a Lagrangian ocean analysis framework for the petascale age. *Geosci. Model Dev.* **10**, 4175–4186 (2017).

58. van Sebille, E. et al. Lagrangian ocean analysis: fundamentals and practices. *Ocean Model.* **121**, 49–75 (2018).

59. Zheng, Y. & Giese, B. S. Ocean heat transport in Simple Ocean data assimilation: structure and mechanisms. *J. Geophys. Res. Oceans* **114**, C11009 (2009).

60. Kim, Y. S. & Orsi, A. H. On the variability of Antarctic Circumpolar Current fronts inferred from 1992-2011 altimetry. *J. Phys. Oceanogr.* **44**, 3054–3071 (2014).

Author contributions
C.J.P. designed the study with input and supervision from G.E.M., A.F.T., L.D.T., and S.T.G. M.R.M. developed the model and G.A.M. configured the Lagrangian particle release experiments. C.J.P. and R.Q.P. conducted the rest of the analysis. R.Q.P. received additional supervision from G.A.M. and S.M.G. R.M. provided code and insights on the overall framing of the work. C.J.P. wrote the manuscript. All authors contributed to the interpretation of the results and commented on the manuscript.

Competing interests
The authors declare no competing interests.

Additional information
Supplementary information The online version contains supplementary material available at https://doi.org/10.1038/s43247-024-01207-y.

Correspondence and requests for materials should be addressed to Channing J. Prend.

Peer review information *Communications Earth & Environment* thanks Steve Rintoul and the other, anonymous, reviewer(s) for their contribution to the peer review of this work. Primary Handling Editors: Jennifer Veitch, Joe Aslin, and Clare Davis. A peer review file is available.

Reprints and permission information is available at http://www.nature.com/reprints

Publisher's note Springer Nature remains neutral with regard to jurisdictional claims in published maps and institutional affiliations.